Roles for K_2CO_3 doping on elevated temperature CO_2 adsorption of potassium promoted layered double oxides

Xuancan Zhu[a], Chunping Chen[b], Qiang Wang*[c], Yixiang Shi*[a], Dermot O'Hare*[b], Ningsheng Cai[a]

[a] Key Laboratory for Thermal Science and Power Engineer of Ministry of Education, Department of Thermal Engineering, Tsinghua University, Beijing, 10084, China. E-mail: shyx@mail.tsinghua.edu.cn; Tel: +86 13810028501

[b] Chemistry Research Laboratory, Department of Chemistry, University of Oxford, 12 Mansfield Road, Oxford, OX1 3TA, UK. E-mail: dermot.ohare@chem.ox.ac.uk; Tel: +44 1865 285130; Fax: +44 1865 285131

[c] Environmental Functional Nanomaterials (EFN) Laboratory, College of Environmental Science and Engineering, Beijing Forestry University, Beijing, 100083, China. E-mail: qiangwang@bjfu.edu.cn; Tel: +86 13699130626

Abstract

Despite the great attraction of using potassium promoted magnesium-aluminum layered double oxides (K-LDOs) as elevated temperature CO_2 adsorbents, the understanding of CO_2 adsorption mechanism of K-LDOs is still confusing and controversial due to the complexity of adsorbent compositions. In this work, in situ techniques were adopted to verify the synergistic mechanism of K_2CO_3 doping (0–40 wt.%) and Mg/Al mole ratio (0.55, 2.17, and 2.98) on the CO_2 capture of K-LDOs. Before K_2CO_3 doping, the commercially available MG63 ($[Mg_{0.69}Al_{0.31}(OH)_2](CO_3)_{0.16}{\cdot}zH_2O$) exhibited the highest working CO_2 capacity of 0.320 mmol/g at 400 °C and 1 atm. After doping with 20 wt.% K_2CO_3, K_{20}-MG70 (Mg/Al ratio: 2.98) gave highest CO_2 capacity of 0.722 mmol/g. At low CO_2 partial pressures, however, K_{20}-MG30 (Mg/Al ratio: 0.55) with the lowest Mg/Al ratio owned the best capture performance. Results from in situ Fourier transform infrared spectroscopy indicate that the changeable CO_2 adsorption performance of K-LDOs was controlled by two mechanisms. For K-LDOs with high Mg/Al ratios, the K_2CO_3 doping is mainly localized in the bulk phase, and acts as a reactant to form high stable K-Mg double carbonates after adsorbing CO_2. With increasing the Al content, surface modification occurs and becomes the dominant enhancement mechanism via the interaction between K^+ and unsaturated oxygen sites, which are generated by the partial substitution of Mg^{2+} with Al^{3+}. The reversible formation of bidentate carbonates are the main CO_2 species on K-Al_2O_3, K-LDOs, and K-MgO, whereas unidentate carbonates with a stronger binding affinity are only formed on K_{20}-MG30, providing a superior performance for the adsorption of low

concentration CO_2.

Keywords

Layered double oxides; Elevated-temperature CO_2 adsorption; Adsorption mechanism; Potassium impregnation; In situ FTIR

GRAPHICAL ABSTRACT

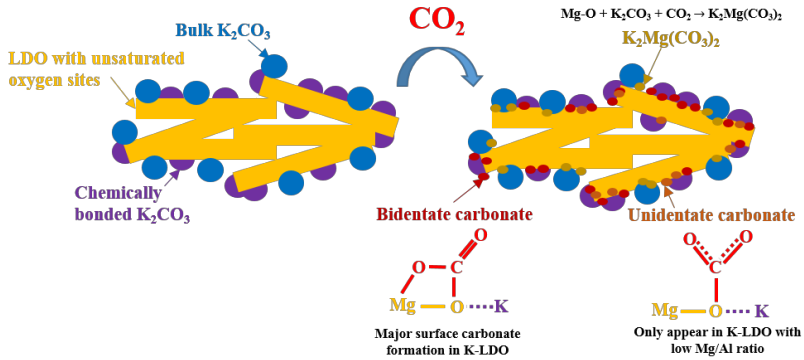

1. Introduction

There is a growing concern that the anthropogenic emission of carbon dioxide is causing the global climate change [1]. Note that the world's energy is still dominated by fossil fuels such as coal, oil, and natural gas, new technologies for CO_2 capture, storage, and utilization (CCUS) are necessary to mitigate the carbon emissions [2]. Layered double hydroxides (LDHs) are excellent precursors for the preparation of elevated-temperature CO_2 adsorbents that have been widely applied in pre-combustion carbon capture [3–5], sorption-enhanced reactions [6,7], and high-purity hydrogen production from fossil fuels [8,9]. Compared with low temperature physical adsorbents [10–12] and high temperature chemical adsorbents [13,14], LDH-derived CO_2 capture materials with weak chemisorption sites have advantages such as high CO_2 adsorption ability at elevated temperatures (200–450 °C), fast adsorption/desorption kinetics, and long-term operation stability [15]. The molecular formula of LDH is given by $\left[M_x^{2+}M^{3+}(OH)_{2(x+1)}\right][A^{n-}]_{1/n}\cdot zH_2O$, where M^{2+} and M^{3+} are metal cations and A^{n-} is the charge-compensating anion. Among different types of LDHs, MgAl-CO_3 is the most common precursor for elevated temperature CO_2 adsorption [16–19].

The crystal structure of LDH consists of positively charged brucite-like layers separated by anionic interlayer galleries. During calcination, the crystalline layered structure of LDHs is destroyed by calcination due to dehydration (70–190 °C), dehydroxylation and decarbonation (190–508 °C) [20], forming amorphous layered double oxides (LDOs) with abundant surface basicity including low- (OH^- groups), medium- (Mg-O pairs), and high-basicity (O^{2-} anions) [21]. The unsaturated oxygen sites from Mg-O pairs and

O^{2-} anions are the predominant CO_2 adsorption sites at elevated temperatures [22], which are formed either by the substitution of Mg^{2+} with Al^{3+} or by the Al^{3+} migration from the lattice sites during calcination [23].

Rodrigues and co-workers systematically studied the correlation between morphology (pore structure, interlayer space, and charge density) and CO_2 adsorption performance of LDOs [15,24–27]. MgAl-CO_3 with different Mg/Al mole ratios (0.55, 1.28, and 2.98), interlayer anionic species (CO_3^{2-} and OH^-), and adsorption temperatures (20, 200, and 300 °C) has been tested [25]. The commercial MG50 with a Mg/Al ratio of 1.28 showed the highest CO_2 adsorption capacity of 0.41 mmol/g at 300 °C and 1 atm CO_2. The CO_2 adsorption capacity of LDOs can be enhanced by impregnating with alkali metal carbonates such as K_2CO_3 and $CsCO_3$ [24]. After doping 20 wt.% K_2CO_3, the CO_2 adsorption capacity of MG30 (Mg/Al ratio: 0.55) increased from 0.10 mmol/g to 0.76 mmol/g (403 °C, 0.4 atm). Wang et al. investigated the effect of trivalent cations (M^{3+} = Al, Fe, Ga, and Mn) [28] and interlayer anions (CO_3^{2-}, HCO_3^-, NO_3^-, SO_4^{2-}, and Cl^-) [29] on the CO_2 adsorption capacity of Mg-M^{3+} based LDOs. They proved that due to its excellent thermal stability and high surface area, Mg_3Al-CO_3 obtained the optimal CO_2 adsorption capacity (0.53 mmol/g at 200 °C and 1 atm). After impregnating 20 wt.% K_2CO_3, the CO_2 adsorption of Mg_3Al-CO_3 was further increased to 0.81 mmol/g [29].

Attempts have been reported to understand the CO_2 adsorption behavior of K-LDOs [24,30–34]. Ding et al. [30] claimed that the CO_2 adsorption of K-LDOs at elevated temperatures was a combination of physisorption and chemisorption, which could be described by Langmuir model and linear driving force (LDF) model. Later, Oliveira et

al. [24] proposed a bi-Langmuir model with an exothermic physisorption process and an endothermic chemisorption process. Lee et al. [31] suggested that a multi-chemisorption process occurred at CO_2 partial pressures above 0.2 atm. On the other hand, Ebner et al. [32,35], Zheng et al. [33], and Silva et al. [34] reported that the CO_2 adsorption of K-LDOs was determined by several highly-coupled and totally-reversible surface reactions.

The above conclusions are mainly based on CO_2 adsorption experiments and so the surface speciation has not been directly validated. Therefore, in situ analytical techniques are required to gain further insight into the enhancement mechanism of K_2CO_3 doping on K-LDOs. In situ Fourier transform infrared spectroscopy (FTIR) is an efficient method to monitor the change of surface functional groups during adsorption and desorption. The IR band for the free carbonate ion is 1415 cm^{-1} (ν_3 vibration), where the band is splitted into two bands on both sides of 1415 cm^{-1} in the adsorbed state due to lowered symmetry. The $\Delta\nu_3$ splitting can tell the type of surface carbonates and the basic strength of adsorption sites. In-situ FTIR results from Du et al. [36] for the CO_2 adsorption of K_2CO_3 promoted Mg_2Al-CO_3 revealed that several reversible processes and one irreversible process occurred. During 300 min adsorption, reversible surface bridged ($\Delta\nu_3$ = 390 cm^{-1}), bidentate ($\Delta\nu_3$ = 253 cm^{-1}), and unidentate carbonates ($\Delta\nu_3$ = 125 cm^{-1}) were formed. The formation of bidentate carbonate was favored and continued during the adsorption step, but the bridged and unidentate carbonates started to transform into irreversible bulk polydentate carbonate ($\Delta\nu_3$ = 70 cm^{-1}) after 60 min of adsorption. Walspurger et al. [37] observed a similar $\Delta\nu_3$ splitting

on the 22 wt.% K_2CO_3 impregnated Al_2O_3 ($\Delta\nu_3$ = 198 cm^{-1}) and $Mg_{2.33}Al$-CO_3 ($\Delta\nu_3$ = 190 cm^{-1}) after CO_2 adsorption, and thus concluded that K^+ creates new adsorption sites by reaction with Al-O centres. However, in situ FTIR results from Zhang et al. [38] indicated that the CO_2 adsorption sites of K_2CO_3 promoted Mg_3Al-CO_3 are the new Lewis adsorption sites Mg(Al)-O-K and Mg-O-K, and the CO_2 adsorption mechanisms varies with K_2CO_3 loading ratios. Recently, Coenen et al. [39] used in situ FTIR to study the CO_2 adsorption on commercial K-MG30 in the presence of 5% steam, and claimed that the CO_2 adsorption only forms reversible bidentate carbonates ($\Delta\nu_3$ = 235 cm^{-1}). However, the CO_2 adsorption sites of K-MG30 are heterogeneous, as the $\Delta\nu_3$ splitting decreased after desorbing with N_2 purge ($\Delta\nu_3$ = 220 cm^{-1}) and steam purge ($\Delta\nu_3$ = 180 cm^{-1}).

The disagreement for the CO_2 adsorption mechanism of K-LDOs might be due to the adoption of various compositions (Mg/Al ratio and K_2CO_3 loading ratio), synthesis procedures of LDH precursors, and testing gases with different CO_2 partial pressures. There are evidences suggesting that the Mg/Al ratio and K_2CO_3 doping work cooperatively and together play an important role in the CO_2 adsorption of K-LDOs. For instance, although previous researchers concluded that there is an optimal Mg/Al molar ratio between 1.3 and 3.5 for the CO_2 adsorption of Mg-Al-CO_3 [23,25,40], Coenen et al. [41] recently found that the CO_2 adsorption capacity of 20 wt.% K_2CO_3-impregnated Al_2O_3 and Mg-Al-CO_3 LDOs (Mg/Al ratios: 0.55 and 2.98) at 400 °C increases with increased Mg/Al ratios. In fixed-bed scale tests, significant amount of residual CO_2 impurities was observed in the product hydrogen before breakthrough

when alkali metal promoted MgO or LDOs with a high Mg/Al ratio were adopted as CO_2 adsorbents [42–44]. However, Zhu et al. [8,9] found that the thermodynamically balanced CO_2 pressure of K-MG30 at 400 °C can be lower than 92×10^{-6} atm. To the best of our knowledge, the cooperative effects of Mg/Al ratio and K_2CO_3 doping on the nature of the CO_2 adsorption sites in K-LDOs has not yet been considered.

To clarify the roles of K_2CO_3 doping on LDOs, K_2CO_3-impregnated Al_2O_3, MgO, and LDOs with different Mg/Al ratios (0.55, 2.17, 2.98) were synthesized and comprehensively characterized in this work. The CO_2 adsorption performance of samples at 400 °C was investigated in terms of working capacity, adsorption/desorption kinetics and isotherms. To examine the CO_2 adsorption mechanism, the adsorption/desorption process on K_2CO_3-impregnated samples including K-Al_2O_3, K-MG30, K-MG70, and K-MgO was monitored by in situ FTIR. The basic strength of the CO_2 adsorption sites in K-LDOs was also evaluated by thermal programmed desorption (TPD).

2. Materials and methods

2.1. Sample preparation

Al_2O_3 (99.7% purity, Sinopharm Chemical Reagent Co., Ltd., China), MgO (98.5% purity, Sinopharm Chemical Reagent Co., Ltd., China), and three commercial LDHs, namely, MG30 (Mg/Al ratio: 0.55), MG63 (Mg/Al ratio: 2.17), and MG70 (Mg/Al ratio: 2.98) (Sasol, Germany), were used as precursors. Typically, 10 g of sample was added to 50 mL of an aqueous solution containing a specific amount of K_2CO_3 or deionized (DI) water for non-impregnated samples. The mixture was then stirred for 1 h at room

157 temperature, dried in an oven for 3 h at 120 °C, and calcined in a muffle furnace for 3
158 h at 450 °C. The synthesized samples were designated as K_A-B, where A represents the
159 K_2CO_3 loading (10, 20, 30, or 40 wt.%) and B is the precursor (Al_2O_3, MgO, MG30,
160 MG63, or MG70). For the water scrubbing process, the calcined samples were washed
161 with DI water until pH 7, and was redried/recalcined. Samples subjected to water
162 scrubbing were designated as K_A-B(w).

163 **2.2. Sample characterisation**

164 The crystal structure of samples was analysed by XRD using an X'Pert Pro MPD
165 diffractometer (Philips, Holland) with Cu K_α radiation. The accelerating voltage and
166 current were 40 kV and 40 mA, respectively. The diffraction patterns were recorded in
167 the range 10°–90° with a step size of 0.02°. The nitrogen BET specific surface area and
168 pore size of samples were measured using a 3H-2000PS analyser (Beishide, China).
169 Prior to analysis, samples were degassed at 150 °C overnight. The surface areas $\boldsymbol{S_{BET}}$
170 and average pore diameters $\boldsymbol{D_p}$ were calculated based on the BET method, whereas
171 the pore volumes $\boldsymbol{V_p}$ between 2 nm and 90 nm were measured using the Barrett–
172 Joyner–Halenda desorption method. The micropore volumes $\boldsymbol{V_{micro}}$ were calculated
173 using the T-plot method. The morphologies and elementary distributions were detected
174 via MERLIN compact scanning electron microscope (SEM) equipped with an Oxford
175 energy dispersive spectroscopy (EDS). Sample powders were sprayed with platinum
176 before experiments.

177 **2.3. Evaluation of CO_2 adsorption performance**

178 The CO_2 adsorption/desorption performance was evaluated by thermogravimetric

analysis (TGA) on a Q600 TGA analyser (TA Instruments). Prior to analysis, about 15 mg of adsorbent was placed on a microbalance and calcined in situ at 450 °C for 1 h under a 100 mL/min N_2 flow rate to avoid the reconstruction of samples when exposing to the atmosphere due to the "memory effect" [23]. The temperature of the furnace was then set to the testing temperature (400 °C). After the sample weight became stable, the inlet gas was alternately switched between CO_2 and N_2 at 1 h intervals. A gas flow rate of 300 mL/min was used during analysis to avoid the replacement effect caused by the system dead volume [45]. The CO_2 isotherms at 0–1 atm and 400 °C were measured on a 3H-2000PH instrument (Beishide, China) with 2–5 g of samples using the previously described static volumetric method [46]. The CO_2 working capacity of samples q_{CO_2} was calculated according to the mass variation during the adsorption and desorption processes (Eq. (1)) [41,47].

$$q_{CO_2} = \frac{\mathrm{abs}(\Delta m_{ads}) + \mathrm{abs}(\Delta m_{des})}{2 M_{CO_2} m_{sample}} \quad (1)$$

Where, Δm_{ads} / Δm_{des} represents the weight of adsorbed/desorbed CO_2 during adsorption/desorption process (g), M_{CO_2} represents CO_2 molar mass (mmol/g), and m_{sample} represents the sample initial weight (g). Different with some published works that only adopted the CO_2 adsorption capacity [22,28,31], the capacities of both the adsorption and desorption were considered here, which was more instructive for the application in pressure swing adsorption processes.

2.4. Evaluation of CO_2 adsorption mechanism

In situ FTIR experiments were carried out on a Bruker Tensor 27 analyser (Bruker Optik, Germany) at 4 cm^{-1} resolution and 32 scans. Prior to analysis, the powder sample was

pressed into a wafer of 13 mm diameter and 12 mg/cm^2 thickness. The sample was then introduced into a stainless steel cell with KBr windows and a maximum operating temperature of 1000 °C, and calcined in situ at 450 °C for 1 h under a 60 mL/min He flow rate. After cooling to 400 °C, the IR spectra during adsorption and desorption were recorded by switching the gas between CO_2 and He at 1 h intervals, and the difference spectra were obtained by subtracting the original sample spectra.

CO_2-TPD experiments were carried out using a Q600 TGA instrument. After calcination at 450 °C, the temperature was adjusted to 400 °C and the inlet gas was switched to CO_2 at a flow rate of 100 mL/min for 1 h. Subsequently, the temperature was decreased to room temperature, and the inlet gas was switched again to He at the same flow rate for 30 min to remove the physically adsorbed CO_2. The CO_2-TPD profiles were obtained by increasing the temperature up to 800 °C at a heating rate of 10 °C/min. The thermal decomposition profiles were obtained using the same procedure but without the CO_2 adsorption step.

3. Results and discussion

3.1. Material characterisation

XRD patterns of K_{20}-Al_2O_3, K_{20}-MG30, K_{20}-MG63, K_{20}-MG70, and K_{20}-MgO were shown in Fig. 1(a), and patterns of Al_2O_3, K_2CO_3, and MgO were shown in Fig. S1 (Supporting Information, the same below). The results reveal that K_{20}-MgO kept a well-crystallized MgO structure after calcination, whereas all K-LDOs showed majority amorphous structures with low intensity MgO Bragg reflections due to the collapse of layered structures [20]. The MgO Bragg reflections in K-LDOs shifted to higher 2θ

223 angles and their intensity decreased with the increased Al content, which was an
224 evidence that the octahedral Mg^{2+} ions in MgO structures were partially substituted by
225 Al^{3+}. In addition, peaks for bulk K_2CO_3 were more clearly observed in the pattern of
226 K_{20}-MgO, probably due to the well-crystallized structure reduced the chemical
227 incorporation and dispersion of K_2CO_3 in the sample surface. The surface area and pore
228 volume of non-impregnated and impregnated samples calculated by N_2 adsorption-
229 desorption isotherms at 77 K were shown in Fig. 1 (b) and (c), respectively. All the
230 samples exhibited a type IV isotherm according to the IUPAC classification, in
231 agreement with the literature data [22,45]. LDOs/K-LDOs and MgO/K-MgO showed
232 no adsorption limitations at relatively high pressures, which is typical of the H3
233 hysteresis loop observed for plate-like particles with slit-shaped pores. Al_2O_3/K-Al_2O_3
234 showed an H4 hysteresis loop, which is commonly associated with narrow slit-shaped
235 pores.
236 Table 1 lists the textural properties of samples including the surface areas, average pore
237 sizes, and pore volumes. As expected, all samples were mesoporous materials with very
238 limited micropore volumes. Interestingly, the increased surface area of LDOs with the
239 increased Al content might indicate the partial substitution of Mg^{2+} with Al^{3+} created
240 more defects on the octahedral MgO structures (Fig. 1 (d)). The surface area and pore
241 volume of all samples rapidly decreased after K_2CO_3 impregnation, which was due to
242 the blockage of small pores by K_2CO_3 [48].
243 **Fig. 1. (a) XRD patterns of 20 wt.% K_2CO_3 impregnated samples after calcination**
244 **at 450 °C; (b) N_2 adsorption-desorption isotherms for non-impregnated samples;**

(c) N_2 adsorption-desorption isotherms for K_2CO_3 impregnated samples; (d) BET surface area for non-impregnated samples.

Table 1. Textural properties of the samples.

Fig. S2 and Fig. 2 shows SEM and EDS results of Al_2O_3, MG30, MG63, MG70, and MgO with and without K_2CO_3 doping, respectively. The slit-shaped morphologies of all K_2CO_3-impregnated samples agreed well with the conclusions of N_2 adsorption isotherms. One obvious difference after K_2CO_3 doping was that some needle-like species was formed on the surface of samples, and could be more clearly observed when increasing the K_2CO_3 loading ratios (Fig. 2(c)). This species was also confirmed by other researchers, which belonged to the bulk K_2CO_3 [24,49]. On the other hand, EDS results indicate that the K element was detected not only in the bulk phase but also throughout the whole surface of particles. Therefore, it was deduced that the impregnated K_2CO_3 also participated the surface modification.

Fig. 2. SEM image and K distribution of (a) K_{20}-Al_2O_3; (b) K_{20}-MG30; (c) K_{40}-MG30; (d) K_{20}-MG63; (e) K_{20}-MG70; (f) K_{20}-MgO.

3.2. Characterisation of CO_2 adsorption/desorption performance

Fig. 3 shows the CO_2 adsorption results of Al_2O_3, LDOs, and MgO before and after K_2CO_3 doping. Before impregnation, LDOs exhibited higher CO_2 working capacities at 400 °C than both Al_2O_3 and MgO (Fig. 3(a),). Although the Mg-O sites are supposed as the main CO_2 adsorption sites of Mg-Al-CO_3 [50], the working capacity of pure MgO at elevated temperatures was very low due to its slow kinetics and high CO_2 thermodynamic equilibrium pressures at temperatures above 300 °C [51]. On the other

hand, Al-O sites were not the main CO_2 adsorption sites for LDOs as demonstrated by the poor CO_2 working capacity of pure Al_2O_3. Therefore, the introduction of Al^{3+} in LDOs was assumed to change the CO_2 adsorption basicity of Mg-O, making it more reactive toward CO_2. Among all three types of LDOs, MG63 with a Mg/Al ratio of 2.17 showed the highest working capacity of 0.320 mmol/g. In fact, previous work exhibited the same trend in the CO_2 adsorption capacity of LDOs [25]. Considering the three types of LDOs have a similar CO_2 adsorption/desorption kinetics, which will be discussed below, the finding in Fig. 3(a) agreed well with previously reported results. The decrease in CO_2 working capacity with further decreasing Mg/Al ratio lower than 2.17 might be attributed to the decrease in total Mg-O adsorption sites. Fig. 3(b) shows the effect of K_2CO_3 loading ratios on the CO_2 working capacity. The CO_2 working capacity of K-MG30 after impregnation with 20 wt.% K_2CO_3 reached the highest value of 0.624 mmol/g. Further increasing the K_2CO_3 loading resulted in a decrease in CO_2 working capacity to 0.430 mmol/g (40 wt.%) that we ascribe to blockage of the mesopores within the LDO by K_2CO_3 (Table 1). Therefore, the K_2CO_3 loading ratio was fixed at 20 wt.% in this study.

Fig. 3. CO_2 working capacity at 400 °C of (a) samples with different Mg/Al ratios, (b) MG30 with different K_2CO_3 impregnation ratios, (c) 20 wt.%-impregnated samples with different Mg/Al ratios, and (d) 20 wt.%-impregnated samples at 0.01 atm CO_2 partial pressure.

Fig. 3(c) shows that after K_2CO_3 impregnation, the CO_2 working capacity of all the samples (Al_2O_3, LDOs, and MgO) was 2–5 times larger than that of non-impregnated

289 samples. Unlike non-impregnated samples, the CO_2 working capacity showed a
290 positive correlation with the total number of Mg-O adsorption sites. The K_{20}-MgO with
291 the highest Mg content owned the highest CO_2 working capacity of 0.883 mmol/g. The
292 improvement of CO_2 capture ability of LDOs after alkali carbonates impregnation was
293 commonly observed by researchers. Table 2 compared the CO_2 adsorption capacity of
294 LDOs and K-LDOs between this work and literatures. Considering alkali carbonates
295 have no CO_2 working capacity at elevated temperatures (Fig. S3), the remarkable
296 enhancement effect upon K_2CO_3 impregnation on LDOs needs further in-depth study.

297 **Table 2. Comparison of CO_2 adsorption capacities of LDOs at temperature T and**
298 **CO_2 partial pressure p_{CO_2} before and after K_2CO_3 impregnation.**

299 Subsequently, the CO_2 working capacities of K_{20}-Al_2O_3, K_{20}-LDOs, and K_{20}-MgO were
300 measured using an inlet gas mixture composing of 1% CO_2 in N_2. As shown in Fig. 3(d),
301 despite having the largest CO_2 working capacity at 1 atm, the K_{20}-MgO showed the
302 lowest value at low CO_2 partial pressures, whereas the K-LDO with the lowest Mg/Al
303 ratio, K_{20}-MG30, exhibited the highest CO_2 working capacity of 0.252 mmol/g. The
304 ability to reversibly adsorb/desorb trace amounts of CO_2 is particularly important in the
305 production and purification of high-purity H_2 for fuel cells [9]. Our results suggest that
306 the basicity of the CO_2 adsorption sites in K-LDOs was largely affected by both Mg/Al
307 ratio and K_2CO_3 impregnation; specifically the partial replacement of Mg^{2+} with Al^{3+}
308 combined with K_2CO_3 impregnation may create stronger CO_2 adsorption sites with
309 higher thermodynamic stability after adsorbing CO_2.

310 The CO_2 adsorption/desorption kinetics of samples was analysed using normalized CO_2

311 uptakes (Fig. S4) at 400 °C. All non-impregnated samples showed similar normalized
312 kinetics (except for the faster initial desorption rate of Al_2O_3), with about 80% of
313 desorption ratio after 60 min of desorption. After impregnating K_2CO_3, the adsorption
314 kinetics of K_{20}-Al_2O_3 and K_{20}-MgO increased and reached an equilibrium after 20 min
315 adsorption, whereas the CO_2 adsorption on K-LDOs continued during the whole
316 adsorption process. The adsorption kinetics of K-LDOs conforms to an Elovich-type
317 behavior owing to the heterogeneity of the adsorption sites [22]. The desorption curves
318 of impregnated samples show that CO_2 was more difficult to desorb from K-LDOs with
319 higher Al content, which is in agreement with the results in Fig. 3.
320 The CO_2 isotherms of K_{20}-Al_2O_3, K_{20}-MG30, and K_{20}-MgO between 0 and 1 atm were
321 measured (Fig. 4). The relationship of CO_2 working capacities for the three adsorbents
322 at high and low partial pressures were consistent with the TGA results shown in Fig.
323 3(c) and (d). The CO_2 working capacity of K_{20}-MgO had a fast increase between 0 and
324 0.8 atm and the increase rate slowed down after 0.8 atm. Considering the
325 thermodynamic equilibrium temperature for the carbonation reaction of MgO is 303 °C
326 at 1 atm (Fig. S5), the fast increase of CO_2 working capacity below 0.8 atm indicated
327 the change of CO_2 thermodynamically balanced pressure after K_2CO_3 impregnation.
328 **Fig. 4. CO_2 isotherms of K_{20}-Al_2O_3, K_{20}-MG30, and K_{20}-MgO at 400 °C.**
329 **3.3. Mechanistic role of K_2CO_3 impregnation and Mg/Al ratio**
330 In situ FTIR experiments were performed to get a deeper insight on the role of K_2CO_3
331 impregnation and Mg/Al ratio in the CO_2 adsorption of K-LDOs. The IR spectra of K_{20}-
332 Al_2O_3, K_{20}-LDOs, and K_{20}-MgO pretreated at 450 °C were recorded and are shown in

Fig. S6. A broad absorption band between 1300 cm^{-1} and 1600 cm^{-1} was observed for all samples, which is due to the overlapping of the ν_3 stretching vibration of surface carbonates and the $2\nu_2$ stretching vibration of bulk K_2CO_3 (1443 cm^{-1}). The vibration at 1414 cm^{-1} was ascribed to the ν_3 stretching mode of free carbonate ions. After coordination with metal ions, the ν_3 stretching band was split into two peaks due to the surface rearrangement of carbonates reduces the symmetry [37]. The appearance of the vibration at 1744 cm^{-1} after K_2CO_3 impregnation was ascribed to the ν_3 vibration of bulk K_2CO_3, and was consistent with the XRD results in Fig. 1(a).

By subtracting the original sample IR spectra, the differential IR spectra of 20 wt.% K_2CO_3-impregnated samples during CO_2 adsorption/desorption at 400 °C were obtained in Fig. 5, and those for non-impregnated samples were shown in Fig. S7. Table 3 lists the IR bands for K_2CO_3-impregnated samples in literatures and this work. Before K_2CO_3 doping, all the samples exhibited very weak vibrations for bidentate carbonates with a similar $\Delta\nu$ of 372–389 cm^{-1}. Additional vibrations with a $\Delta\nu$ of 295 cm^{-1} appeared in MgO, which also belonged to bidentate carbonates but with stronger bonding strength. After K_2CO_3 doping, changes in the IR difference spectra were more clearly observed owing to enhanced CO_2 capacities. Vibrations at 1626 cm^{-1} and 1290 cm^{-1} with a $\Delta\nu$ of 336 cm^{-1} for K_{20}-MgO can be ascribed to the asymmetric and symmetric stretching of bidentate carbonate. These vibrations appeared immediately after adsorption, increased with adsorption time but at a slower increasing rate, and were still observed after 60 min desorption, which was consistent with the change of CO_2 uptakes. Interestingly, negative bands were observed near the characteristic vibrations of bulk

K_2CO_3, indicating that some of bulk K_2CO_3 participated in the CO_2 adsorption. This is in agreement with the results of in situ XRD study that the improvement of the adsorption performance of MgO after K_2CO_3 was mainly due to the formation of K-Mg double carbonates with higher thermal stability (Eq. (2)) [54,55]. In fact, Duan et al. [56] studied the thermodynamic equilibrium of K_2CO_3-impregnated MgO by ab initio calculations, and concluded that mixing with the metal carbonate increases the CO_2 adsorption temperature of pure MgO.

$$K_2CO_3 + MgO + CO_2 \leftrightarrow K_2Mg(CO_3)_2 \quad (2)$$

Fig. 5. IR difference spectra of samples during CO_2 adsorption/desorption at 0 (within seconds), 1, 3, 5, 10, 20, 40, and 60 min (400 °C, 1 atm).

Table 3. IR bands (cm^{-1}) of K_2CO_3-impregnated samples.

Similar to K_{20}-MgO, the adsorption vibrations of bidentate carbonate at 1643 cm^{-1} and 1279 cm^{-1} were observed in the spectrum of K_{20}-Al_2O_3. These vibrations were weaker than those of K_{20}-MgO due to a lower amount of adsorbed CO_2 of K_{20}-Al_2O_3. The $\Delta\nu$ of the ν_3 vibrations was 364 cm^{-1}, which was larger than that of K_{20}-MgO, but smaller than that of pure Al_2O_3 [57]. In addition, no negative bands were detected for the bulk K_2CO_3. Hence, the promotional effect of K_2CO_3 impregnation on the CO_2 adsorption capacity of Al_2O_3 was only due to surface modification. The K^+ ions reacted with Al_2O_3 to form new adsorption sites that have a higher affinity to CO_2, as the coordination with K^+ ions having low polarisation energy increased the symmetry of the ν_3 bands.

The vibrational bands of bidentate carbonates at 1603 cm^{-1} and 1302 cm^{-1} were detected in the spectrum of K_{20}-MG70. The $\Delta\nu$ value of 301 cm^{-1} was lower than that

observed in the spectra of Al-O and Mg-O but higher than that of K-O [38], suggesting that K^+ reacted with the surface of MG70 to form K-O-Mg adsorption sites. Compared to MgO with a perfect crystal structure, a higher amount of unsaturated oxygen has been reported on the surface of MG70 due to partial replacement of Al^{3+} with Mg^{2+} and escape of Al^{3+} from the lattice sites during calcination [24]. These findings suggest that K^+ reacted more easily with unsaturated oxygen on K_{20}-MG70 to form K-O-Mg adsorption sites. In addition, the negative bands of bulk K_2CO_3 also appeared for K_{20}-MG70, suggesting that the enhancement effect of K_2CO_3 on MG70 might be due to both surface modification and reactivity of bulk K_2CO_3. To verify the above hypothesis, the working capacities of K_{20}-MG70(w) and K_{20}-MgO(w) subjected to water scrubbing after calcination were studied and compared with those of K_{20}-MG70 and K_{20}-MgO (Fig. 6). As expected, for both samples, the working capacity decreased due to the loss of bulk K_2CO_3. However, the decreasing ratio for K_{20}-MG70(w) (44.7%) was smaller than that for K_{20}-MgO(w) (68.3%). Notably, the working capacity of K_{20}-MG70(w) (0.399 mmol/g) was still much higher than that of the corresponding non-impregnated sample (0.195 mmol/g). The IR difference spectra for K_{20}-MG70(w) and K_{20}-MgO(w) in Fig. 7 indicates that the negative bands of bulk K_2CO_3 disappeared after water scrubbing and bidentate carbonates were formed in both samples but with increased $\Delta\nu$ of 350 cm^{-1} for K_{20}-MG70(w) and 363 cm^{-1} for K_{20}-MgO(w). The $\Delta\nu$ value was still lower than that of MG70 (385 cm^{-1}), which suggests that the enhanced working capacity of K-LDOs after water scrubbing compared to those without K_2CO_3 doping was due to the surface modification of the strongly bonded K^+ ions.

Fig. 6. CO_2 working capacity of samples at 400 °C after water scrubbing.

Fig. 7. IR difference spectra of samples after water scrubbing during CO_2 adsorption/desorption at 0 (within seconds), 1, 3, 5, 10, 20, 40, and 60 min (400 °C, 1 atm).

Compared to K_{20}-MG70, the adsorption difference spectrum of K_{20}-MG30 with a higher Al content was more complex. Besides the typical bands of bidentate carbonate (1598 cm^{-1} and 1321 cm^{-1}), vibrations at 1508 cm^{-1} and 1396 cm^{-1} were detected, which could be attributed to the asymmetric and symmetric stretching of more basic unidentate carbonate. The formation of adsorption sites for unidentate carbonate may be responsible for the high adsorption capacity of K_{20}-MG30 at low CO_2 partial pressures. Moreover, no negative bands for bulk K_2CO_3 were observed, indicating that surface modification was the main adsorption enhancement factor for K_{20}-MG30.

The basicity of K_{20}-MG30, K_{20}-MG70, and K_{20}-MgO was studied by CO_2-TPD (Fig. 8). As samples may decompose after 450 °C, the actual CO_2 desorption curve during heating was estimated from the difference spectra between CO_2-TPD and the thermal decomposition spectra. As expected, the maxima of the CO_2 desorption curves of K-LDOs shifted to higher temperatures with increasing the Al content, indicating the higher basicity of CO_2 adsorption sites. The peak width of K_{20}-MG30 was larger than those of K_{20}-MgO and K_{20}-MG70 because of the existence of adsorption sites of both low (bidentate carbonate) and high basicity (unidentate carbonate).

Fig. 8. Difference spectra between the CO_2-TPD and thermal decomposition spectra.

Combined with the above results, a possible CO_2 adsorption route of K-LDOs were illustrated in Fig. 9. The enhancement of K_2CO_3 impregnation on the CO_2 working capacity of LDOs resulted from both the surface modification and the existence of bulk K_2CO_3. In K-LDOs with high Mg/Al ratios, the crystal structures of MgO were well preserved after calcination, which made the easier formation of bulk K_2CO_3. During CO_2 adsorption, the bulk K_2CO_3 participated into the reaction and formed K-Mg double carbonates with higher thermal stability. When reducing the Mg/Al ratio, the partial substitution of Mg^{2+} with Al^{3+} created more unsaturated oxygen on the surface of K-LDOs. The unsaturated oxygen was then reacted with the impregnated K^+ ions, creating K-O-Mg adsorption sites with higher basicity. The adsorbed CO_2 on the surface of K-LDOs mainly formed reversible bidentate carbonates. However, unidentate carbonates would be also formed in K-LDOs when further reducing Mg/Al ratios, which was able to capture extremely low concentration CO_2

Fig. 9. Schematic illustration of the possible CO_2 adsorption routes of K-LDOs.

4. Conclusion

In this work, the CO_2 adsorption mechanism of K-LDOs with different Mg/Al ratios was studied by in situ FTIR. For K_{20}-MG70, the bulk K_2CO_3 on the surface participated into the CO_2 adsorption and formed K-Mg double carbonates with high thermodynamic stability, which allowed the increase of operating temperatures at a given CO_2 partial pressure. On the other hand, the K_2CO_3 doping was also demonstrated to enhance the CO_2 adsorption capacity of K_{20}-MG70 through surface modification. The K^+ ions were speculated to react with the surface unsaturated oxygen, forming K-O-Mg adsorption

sites with higher reaction activity. The surface modification dominated in K-LDOs with a low Mg/Al ratio, probably because of increased unsaturated oxygen sites created by the substituted of Al^{3+}. The basicity of the CO_2 adsorption sites of K-LDOs increased with increasing Al content, and K_{20}-MG30 showed the largest CO_2-TPD peak width due to the existence of both weak (bidentate carbonate) and strong adsorption sites (unidentate carbonate). To the best of our knowledge, the promotion effect of bulk K_2CO_3 on the CO_2 adsorption thermodynamic stability of K-LDOs with high Mg/Al ratios and the reason for the trace CO_2 adsorption ability of K-LDOs with low Mg/Al ratios have not been reported yet. These findings about the synergistic mechanism of K_2CO_3 doping and Mg/Al ratio might provide solutions for the design of efficient CO_2 adsorbents and systems with either/both higher CO_2 working capacities or/and deep purification abilities.

Acknowledgement

This research is financed by Shanxi Province Science and Technology Major Projects of (MH2015-06). The authors express their thanks to Tianjin Xianquan Co., LTD for providing in situ FTIR testing services and Wanlin Gao from Beijing Forestry University for the guidance in FTIR tests.

Reference

[1] D.W. Keith, Why Capture CO_2 from the Atmosphere?, Science 325 (2009) 1654-1655.

[2] M. Bui, C.S. Adjiman, A. Bardow, E.J. Anthony, A. Boston, S. Brown, P.S. Fennell, S. Fuss, A. Galindo, L.A. Hackett, J.P. Hallett, H.J. Herzog, G. Jackson, J. Kemper, S. Krevor, G.C. Maitland, M. Matuszewski, I.S. Metcalfe, C. Petit, G. Puxty, J. Reimer, D.M. Reiner, E.S. Rubin, S.A. Scott, N. Shah, B. Smit, J.P.M. Trusler, P. Webley, J. Wilcox, N. Mac Dowell, Carbon capture and storage (CCS): the way forward, Energ. Environ. Sci. 11 (2018) 1062-1176.

[3] Q. Wang, J. Luo, Z. Zhong, A. Borgna, CO_2 capture by solid adsorbents and their applications: current status and new trends, Energ. Environ. Sci. 4 (2011) 42-55.

[4] J. Wang, L. Huang, R. Yang, Z. Zhang, J. Wu, Y. Gao, Q. Wang, D. O'Hare, Z. Zhong, Recent advances in solid sorbents for CO_2 capture and new development trends, Energ. Environ. Sci. 7 (2014) 3478-3518.

[5] X. Zhu, Y. Shi, N. Cai, Integrated gasification combined cycle with carbon dioxide capture by elevated temperature pressure swing adsorption, Appl. Energ. 176 (2016) 196-208.

[6] Y.J. Wu, P. Li, J.G. Yu, A.F. Cunha, A.E. Rodrigues, Progress on sorption-enhanced reaction process for hydrogen production, Rev. Chem. Eng. 32 (2016) 271-303.

[7] D. Jansen, E. van Selow, P. Cobden, G. Manzolini, E. Macchi, M. Gazzani, R. Blom, P.P. Henriksen, R. Beavis, A. Wright, SEWGS Technology is Now Ready for Scale-up!, Energ. Procedia 37 (2013) 2265-2273.

[8] X. Zhu, Y. Shi, N. Cai, Characterization on trace carbon monoxide leakage in high purity hydrogen in sorption enhanced water gas shifting process, Int. J. Hydrogen Energ. 41 (2016) 18050-18061.

[9] X. Zhu, Y. Shi, N. Cai, CO_2 residual concentration of potassium-promoted hydrotalcite for deep CO/CO_2 purification in H_2-rich gas, J. Energy Chem. 26 (2017) 956-964.

[10] L. Liu, Z.H. Xie, Q.F. Deng, X.X. Hou, Z.Y. Yuan, One-pot carbonization enrichment of nitrogen in microporous carbon spheres for efficient CO_2 capture, J. Mater. Chem. A 5 (2017) 418-425.

[11] Y.J. Zhou, J.J. Liu, M. Xiao, Y.Z. Meng, L.Y. Sun, Designing Supported Ionic Liquids (ILs) within Inorganic Nanosheets for CO_2 Capture Applications, Acs Appl. Mater. Inter. 8 (2016) 5547-5555.

[12] C. Chen, W.-S. Ahn, CO_2 capture using mesoporous alumina prepared by a sol-gel process, Chem. Eng. J. 166 (2011) 646-651.

[13] A. Cruz-Hernandez, J.A. Mendoza-Nieto, H. Pfeiffer, NiO-CaO materials as promising catalysts for hydrogen production through carbon dioxide capture and subsequent dry methane reforming, J. Energy Chem. 26 (2017) 942-947.

[14] P. Olavarria, E. Vera, E.J. Lima, H. Pfeiffer, Synthesis and evaluation as CO_2 chemisorbent of the $Li_5(Al_{1-x}Fe_x)O_4$ solid solution materials: Effect of oxygen addition, J. Energy Chem. 26 (2017) 948-955.

[15] Z. Yong, V. Mata, A.E. Rodrigues, Adsorption of carbon dioxide at high temperature - a review, Sep. Purif. Technol. 26 (2002) 195-205.

[16] S.I. Garces-Polo, J. Villarroel-Rocha, K. Sapag, S.A. Korili, A. Gil, Adsorption of CO_2 on mixed oxides derived from hydrotalcites at several temperatures and high pressures, Chem. Eng. J. 332 (2018) 24-32.

[17] M. De Marco, R. Menzel, S.M. Bawaked, M. Mokhtar, A.Y. Obaid, S.N. Basahel, M.S.P. Shaffer, Hybrid effects in graphene oxide/carbon nanotube-supported layered double hydroxides: enhancing the CO_2 sorption properties, Carbon 123 (2017) 616-627.

[18] X.C. Kou, H.X. Guo, E.G. Ayele, S. Li, Y.J. Zhao, S.P. Wang, X.B. Ma, Adsorption of CO_2 on MgAl-CO_3 LDHs-Derived Sorbents with 3D Nanoflower-like Structure, Energ. Fuel. 32 (2018) 5313-5320.

[19] X. Zhu, Q. Wang, Y. Shi, N. Cai, Layered double oxide/activated carbon-based composite adsorbent for elevated temperature H_2/CO_2 separation, Int. J. Hydrogen Energ. 40 (2015) 9244-9253.
[20] W.S. Yang, Y. Kim, P.K.T. Liu, M. Sahimi, T.T. Tsotsis, A study by in situ techniques of the thermal evolution of the structure of a Mg-Al-CO_3 layered double hydroxide, Chem. Eng. Sci. 57 (2002) 2945-2953.
[21] J.I. Di Cosimo, V.K. Diez, M. Xu, E. Iglesia, C.R. Apesteguia, Structure and surface and catalytic properties of Mg-Al basic oxides, J. Catal. 178 (1998) 499-510.
[22] M. Leon, E. Diaz, S. Bennici, A. Vega, S. Ordonez, A. Auroux, Adsorption of CO_2 on Hydrotalcite-Derived Mixed Oxides: Sorption Mechanisms and Consequences for Adsorption Irreversibility, Ind. Eng. Chem. Res. 49 (2010) 3663-3671.
[23] Y. Gao, Z. Zhang, J. Wu, X. Yi, A. Zheng, A. Umar, D. O'Hare, Q. Wang, Comprehensive investigation of CO_2 adsorption on Mg-Al-CO_3 LDH-derived mixed mental oxides, J. Mater. Chem. A 1 (2013) 12782-12790.
[24] E.L.G. Oliveira, C.A. Grande, A.E. Rodrigues, CO_2 sorption on hydrotalcite and alkali-modified (K and Cs) hydrotalcites at high temperatures, Sep. Purif. Technol. 62 (2008) 137-147.
[25] Z. Yong, V. Mata, A.E. Rodrigues, Adsorption of carbon dioxide onto hydrotalcite-like compounds (HTlcs) at high temperatures, Ind. Eng. Chem. Res. 40 (2001) 204-209.
[26] Z. Yong, A.E. Rodrigues, Hydrotalcite-like compounds as adsorbents for carbon dioxide, Energ. Convers. Manage. 43 (2002) 1865-1876.
[27] R. Moreira, J.L. Soares, G.L. Casarin, A.E. Rodrigues, Adsorption of CO_2 on hydrotalcite-like compounds in a fixed bed, Sep. Sci. Technol. 41 (2006) 341-357.
[28] Q. Wang, H.H. Tay, D.J.W. Ng, L. Chen, Y. Liu, J. Chang, Z. Zhong, J. Luo, A. Borgna, The Effect of Trivalent Cations on the Performance of Mg-M-CO_3 Layered Double Hydroxides for High-Temperature CO_2 Capture, Chemsuschem 3 (2010) 965-973.
[29] Q. Wang, Z. Wu, H.H. Tay, L. Chen, Y. Liu, J. Chang, Z. Zhong, J. Luo, A. Borgna, High temperature adsorption of CO_2 on Mg-Al hydrotalcite: Effect of the charge compensating anions and the synthesis pH, Catal. Today 164 (2011) 198-203.
[30] Y. Ding, E. Alpay, Equilibria and kinetics of CO_2 adsorption on hydrotalcite adsorbent, Chem. Eng. Sci. 55 (2000) 3461-3474.
[31] K.B. Lee, A. Verdooren, H.S. Caram, S. Sircar, Chemisorption of carbon dioxide on potassium-carbonate-promoted hydrotalcite, J. Colloid. Interf. Sci. 308 (2007) 30-39.
[32] A.D. Ebner, S.P. Reynolds, J.A. Ritter, Nonequilibrium kinetic model that describes the reversible adsorption and desorption behavior of CO2 in a K-promoted hydrotalcite-like compound, Ind. Eng. Chem. Res. 46 (2007) 1737-1744.
[33] Y. Zheng, Y. Shi, S. Li, Y. Yang, N. Cai, Elevated temperature hydrogen/carbon dioxide separation process simulation by integrating elementary reaction model of hydrotalcite adsorbent, Int. J. Hydrogen Energ. 39 (2014) 3771-3779.
[34] J.M. Silva, R. Trujillano, V. Rives, M.A. Soria, L.M. Madeira, High temperature CO_2 sorption over modified hydrotalcites, Chem. Eng. J. 325 (2017) 25-34.
[35] A.D. Ebner, S.P. Reynolds, J.A. Ritter, Understanding the adsorption and desorption behavior of CO2 on a K-promoted hydrotalcite-like compound (HTlc) through nonequilibrium dynamic isotherms, Industrial & Engineering Chemistry Research 45 (2006) 6387-6392.
[36] H. Du, C.T. Williams, A.D. Ebner, J.A. Ritter, In Situ FTIR Spectroscopic Analysis of Carbonate Transformations during Adsorption and Desorption of CO_2 in K-Promoted HTlc, Chem. Mater. 22 (2010)

3519-3526.
[37] S. Walspurger, L. Boels, P.D. Cobden, G.D. Elzinga, W.G. Haije, R.W. van den Brink, The Crucial Role of the K^+-Aluminium Oxide Interaction in K^+-Promoted Alumina- and Hydrotalcite-Based Materials for CO_2 Sorption at High Temperatures, Chemsuschem 1 (2008) 643-650.
[38] Y.X. Zhang, Q.Y. Su, Z.P. Wang, X.Y. Gao, Z.L. Zhang, Surface Modification of Mg-Al Hydrotalcite Mixed Oxides with Potassium, Acta Phys.-Chim. Sin. 26 (2010) 921-926.
[39] K. Coenen, F. Gallucci, B. Mezari, E. Hensen, M.v.S. Annaland, An in-situ IR study on the adsorption of CO_2 and H_2O on hydrotalcites, J. CO_2 Util. 24 (2018) 228-239.
[40] U. Sharma, B. Tyagi, R.V. Jasra, Synthesis and Characterization of Mg-Al-CO_3 Layered Double Hydroxide for CO_2 Adsorption, Ind. Eng. Chem. Res. 47 (2008) 9588-9595.
[41] K. Coenen, F. Gallucci, P. Cobden, E. van Dijk, E. Hensen, M.V. Annaland, Influence of material composition on the CO_2 and H_2O adsorption capacities and kinetics of potassium-promoted sorbents, Chem. Eng. J. 334 (2018) 2115-2123.
[42] M.G. Beaver, H.S. Caram, S. Sircar, Selection of CO_2 chemisorbent for fuel-cell grade H_2 production by sorption-enhanced water gas shift reaction, Int. J. Hydrogen Energ. 34 (2009) 2972-2978.
[43] E.R. van Selow, P.D. Cobden, P.A. Verbraeken, J.R. Hufton, R.W. van den Brink, Carbon Capture by Sorption-Enhanced Water-Gas Shift Reaction Process using Hydrotalcite-Based Material, Ind. Eng. Chem. Res. 48 (2009) 4184-4193.
[44] Y. Hu, H. Cui, Z. Cheng, Z. Zhou, Sorption-enhanced water gas shift reaction by in situ CO_2 capture on an alkali metal salt-promoted MgO-$CaCO_3$ sorbent, Chem. Eng. J. DOI: 10.1016/j.cej.2018.08.209.
[45] X. Zhu, Y. Shi, N. Cai, High-pressure carbon dioxide adsorption kinetics of potassium-modified hydrotalcite at elevated temperature, Fuel 207 (2017) 579-590.
[46] P. Hao, Y. Shi, S. Li, S. Liang, Oxygen sorption/desorption kinetics of $SrCo_{0.8}Fe_{0.2}O_3-\delta$ perovskite adsorbent for high temperature air separation, Adsorption 24 (2018) 65-71.
[47] X. Zhu, C. Chen, H. Suo, Q. Wang, Y. Shi, D. O'Hare, N. Cai, Synthesis of elevated temperature CO_2 adsorbents from aqueous miscible organic-layered double hydroxides, Energy 167 (2018) 960-969.
[48] J.M. Lee, Y.J. Min, K.B. Lee, S.G. Jeon, J.G. Na, H.J. Ryu, Enhancement of CO_2 Sorption Uptake on Hydrotalcite by Impregnation with K_2CO_3, Langmuir 26 (2010) 18788-18797.
[49] C.V. Miguel, R. Trujillano, V. Rives, M.A. Vicente, A.F.P. Ferreira, A.E. Rodrigues, A. Mendes, L.M. Madeira, High temperature CO_2 sorption with gallium-substituted and promoted hydrotalcites, Sep. Purif. Technol. 127 (2014) 202-211.
[50] M.K.R. Reddy, Z.P. Xu, G.Q. Lu, J.C.D. da Costa, Influence of water on high-temperature CO_2 capture using layered double hydroxide derivatives, Ind. Eng. Chem. Res. 47 (2008) 2630-2635.
[51] J. Fagerlund, J. Highfield, R. Zevenhoven, Kinetics studies on wet and dry gas-solid carbonation of MgO and $Mg(OH)_2$ for CO_2 sequestration, Rsc Adv. 2 (2012) 10380-10393.
[52] J.I. Yang, J.N. Kim, Hydrotakites for adsorption of CO_2 at high temperature, Korean J. Chem. Eng. 23 (2006) 77-80.
[53] S. Li, Y. Shi, Y. Yang, Y. Zheng, N. Cai, High-Performance CO_2 Adsorbent from Interlayer Potassium-Promoted Stearate-Pillared Hydrotalcite Precursors, Energ. Fuel. 27 (2013) 5352-5358.
[54] C.H. Lee, H.J. Kwon, H.C. Lee, S. Kwon, S.G. Jeon, K.B. Lee, Effect of pH-controlled synthesis on the physical properties and intermediate-temperature CO_2 sorption behaviors of K-Mg double salt-based sorbents, Chem. Eng. J. 294 (2016) 439-446.
[55] W.L. Gao, T.T. Zhou, Y.S. Gao, B. Louis, D. O'Hare, Q. Wang, Molten salts-modified MgO-based adsorbents for intermediate-temperature CO_2 capture: A review, J. Energy Chem. 26 (2017) 830-838.

[56] Y.H. Duan, K.L. Zhang, X.H.S. Li, D.L. King, B.Y. Li, L.F. Zhao, Y.H. Xiao, ab initio Thermodynamic Study of the CO_2 Capture Properties of M_2CO_3 (M = Na, K)- and $CaCO_3$-Promoted MgO Sorbents Towards Forming Double Salts, Aerosol Air Qual. Res. 14 (2014) 470-479.
[57] G. Busca, V. Lorenzelli, Infrared spectrosopic identification of species arising from reactive adsorption of carbon oxides on metal-oxide surfaces, Mater. Chem. 7 (1982) 89-126.

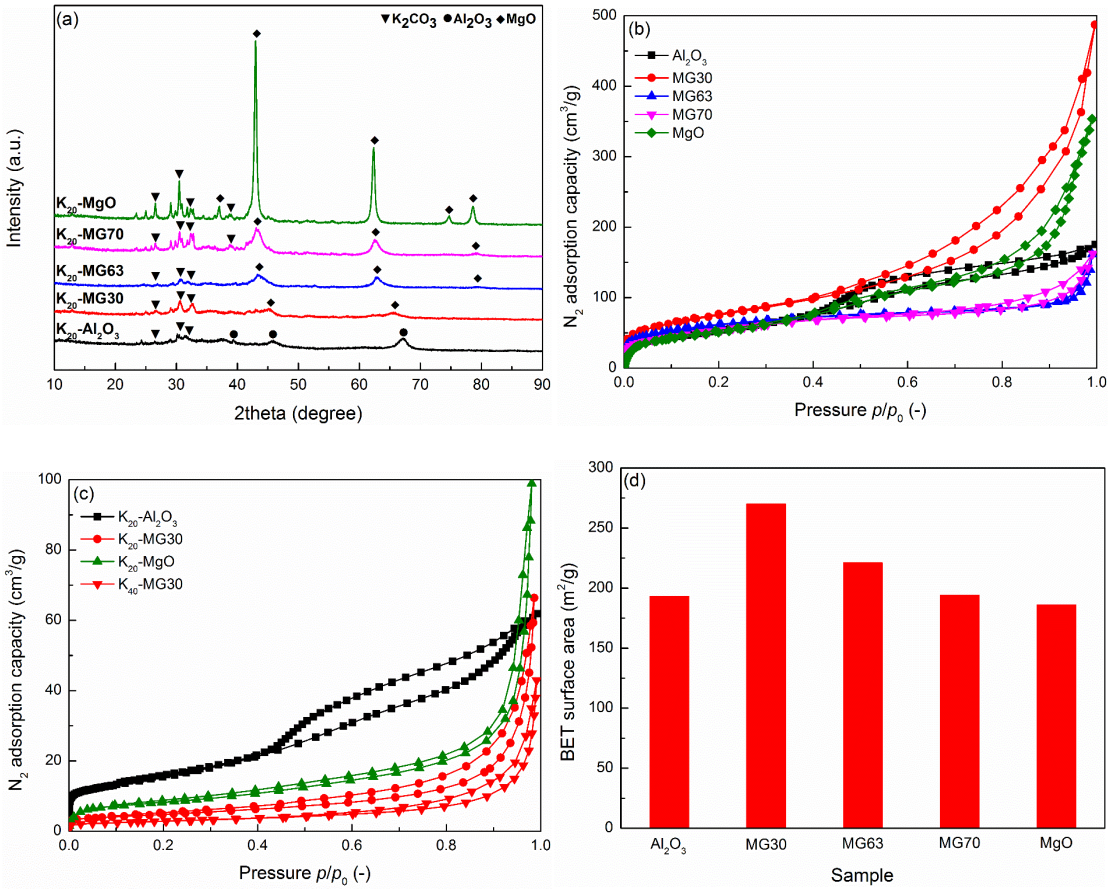

Fig. 1. (a) XRD patterns of 20 wt.% K_2CO_3 impregnated samples after calcination at 450 °C; (b) N_2 adsorption-desorption isotherms for non-impregnated samples; (c) N_2 adsorption-desorption isotherms for K_2CO_3 impregnated samples; (d) BET surface area for non-impregnated samples.

609 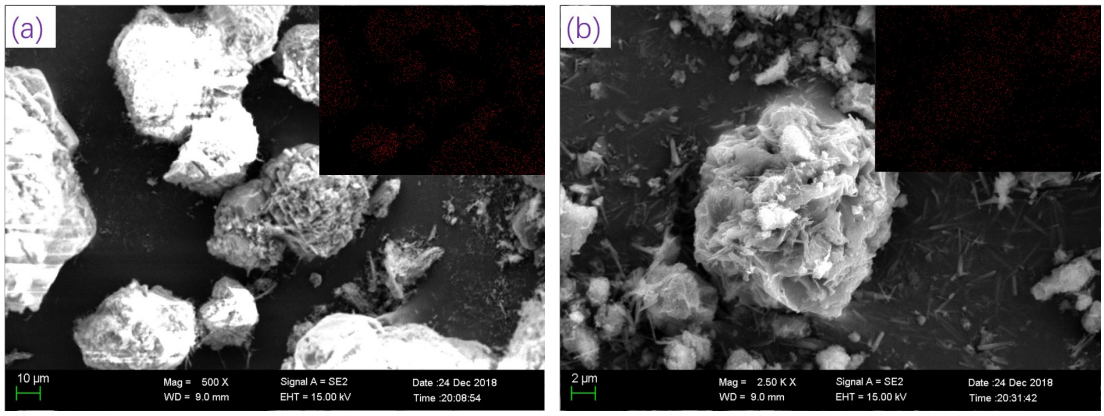

610 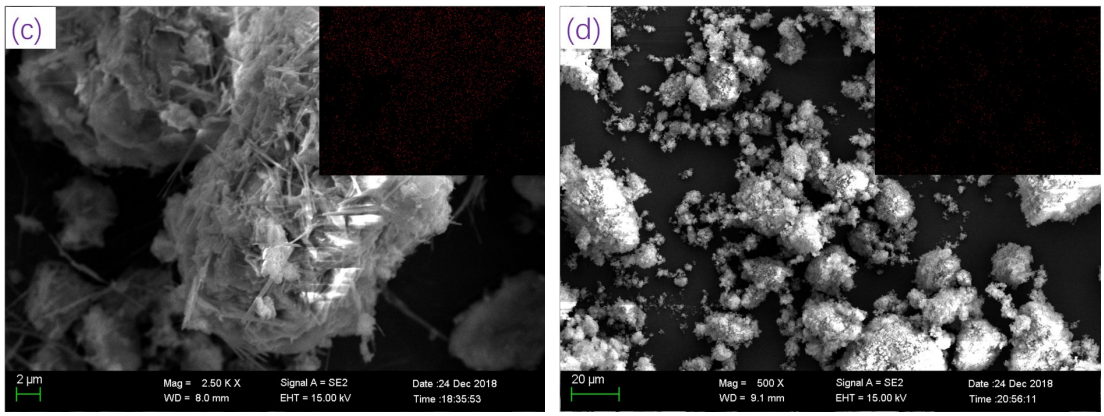

611 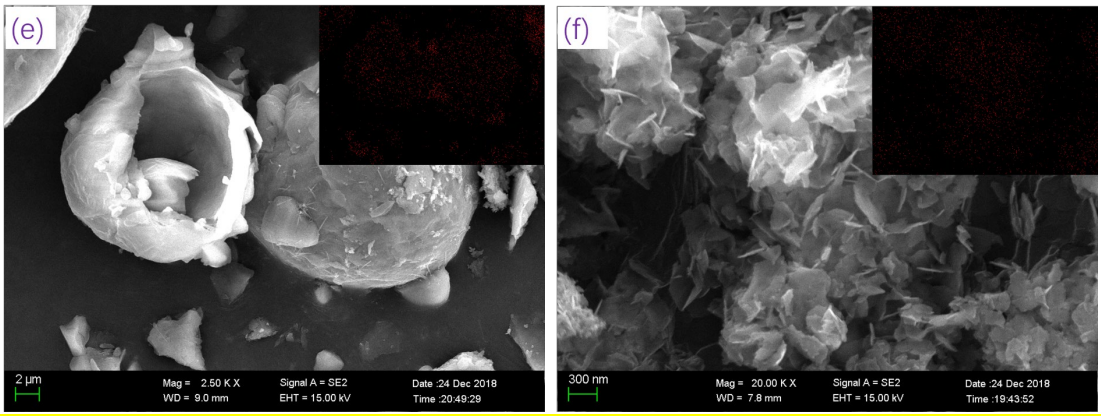

612 **Fig. 2. SEM image and K distribution of (a) K_{20}-Al_2O_3; (b) K_{20}-MG30; (c) K_{40}-**

613 **MG30; (d) K_{20}-MG63; (e) K_{20}-MG70; (f) K_{20}-MgO.**

614

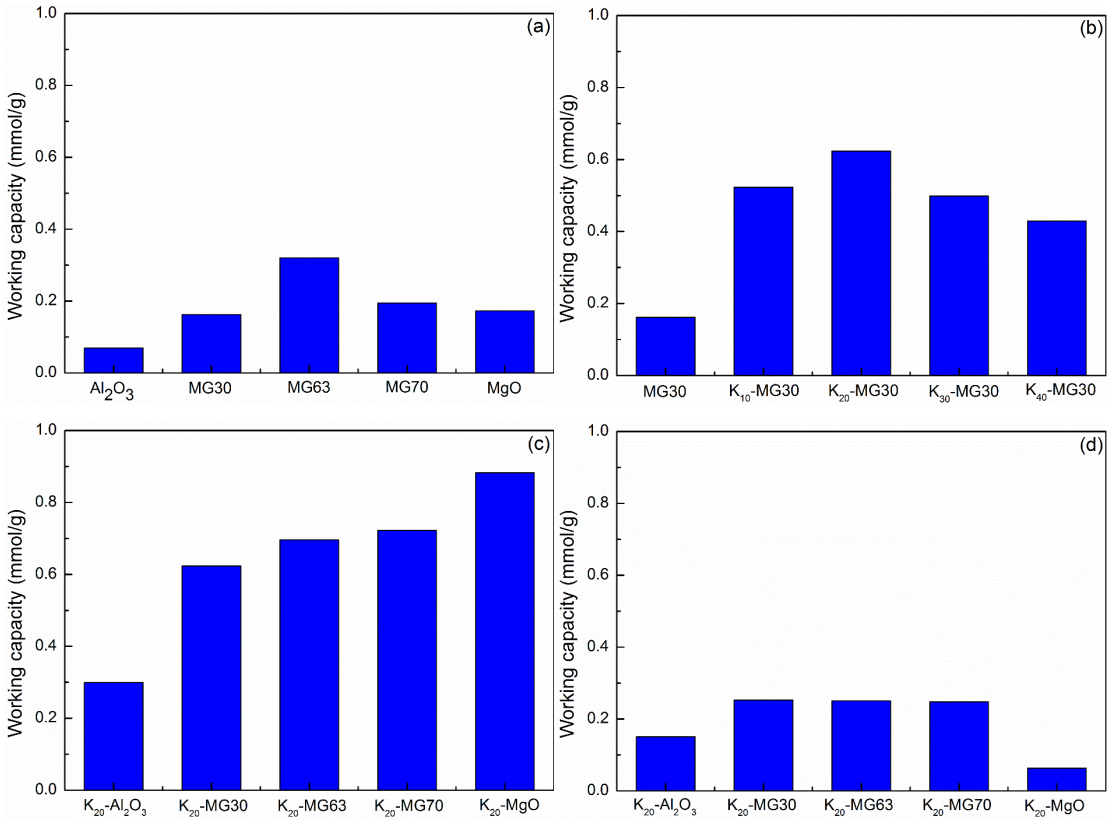

Fig. 3. **CO_2 working capacity at 400 °C of (a) samples with different Mg/Al ratios, (b) MG30 with different K_2CO_3 impregnation ratios, (c) 20 wt.%-impregnated samples with different Mg/Al ratios, and (d) 20 wt.%-impregnated samples at 0.01 atm CO_2 partial pressure.**

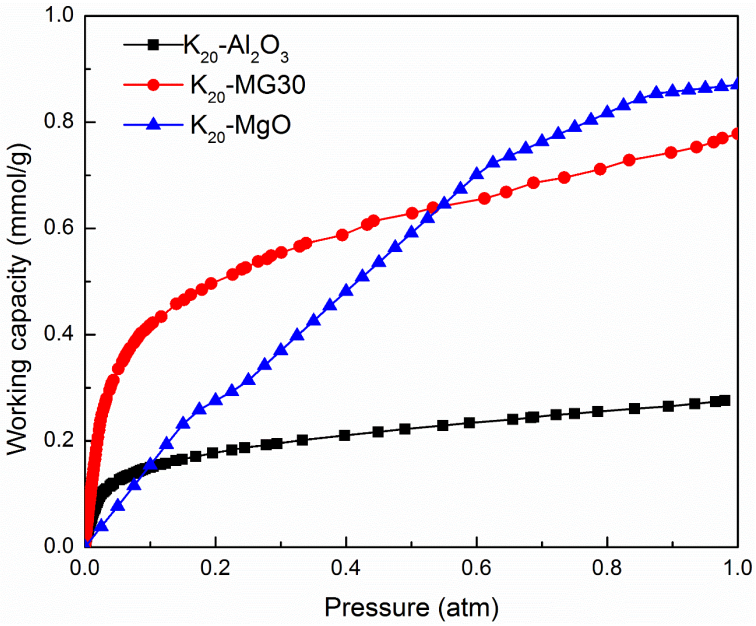

623

624 **Fig. 4. CO_2 isotherms of K_{20}-Al_2O_3, K_{20}-MG30, and K_{20}-MgO at 400 °C.**

625

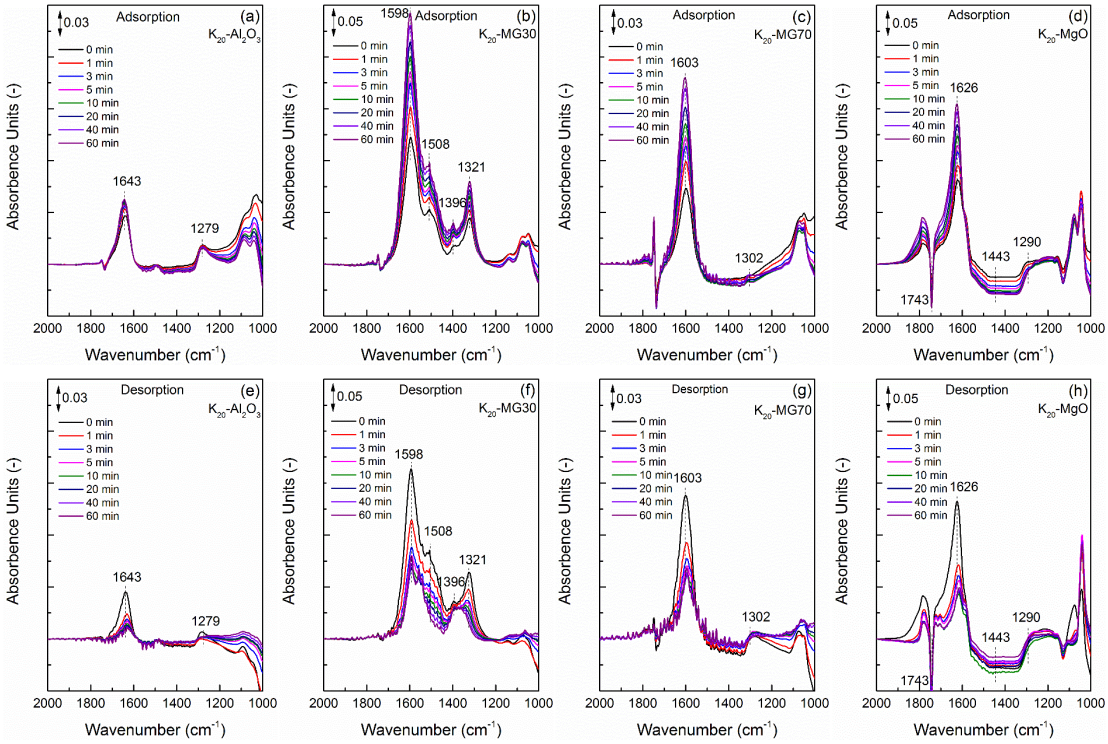

Fig. 5. IR difference spectra of samples during CO_2 adsorption/desorption at 0 (within seconds), 1, 3, 5, 10, 20, 40, and 60 min (400 °C, 1 atm).

632 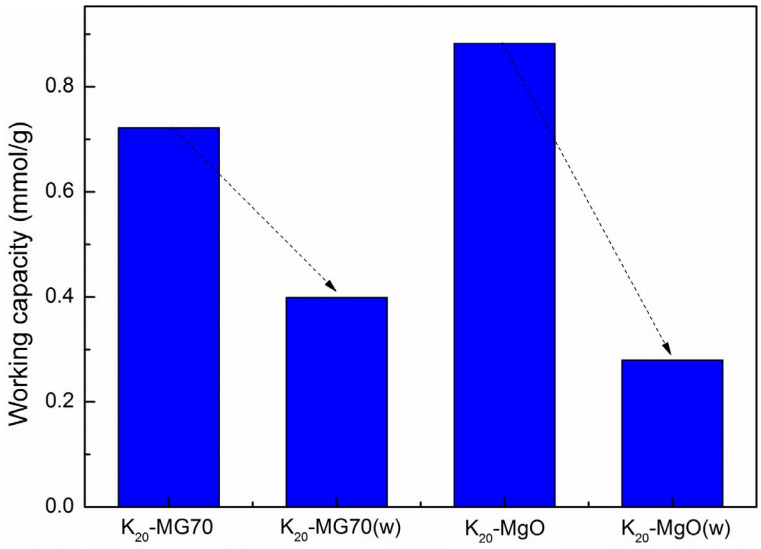

633 **Fig. 6. CO_2 working capacity of samples at 400 °C after water scrubbing.**

634

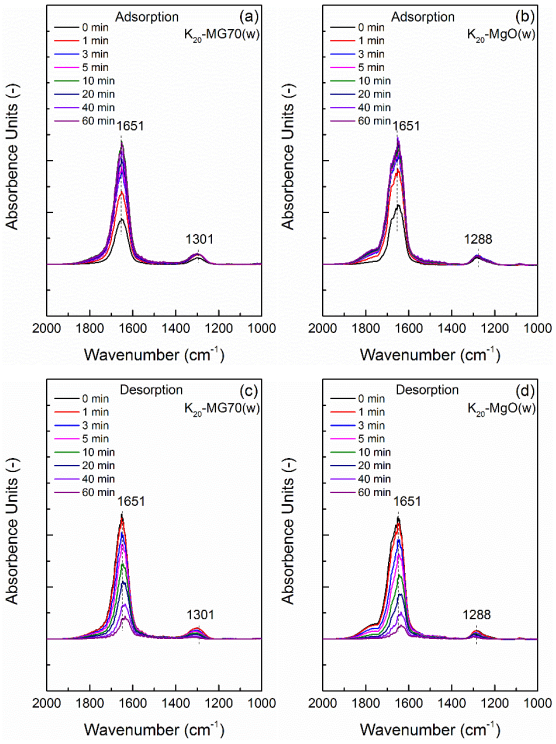

635

636

637 **Fig. 7. IR difference spectra of samples after water scrubbing during CO_2**

638 **adsorption/desorption at 0 (within seconds), 1, 3, 5, 10, 20, 40, and 60 min (400 °C,**

639 **1 atm).**

640

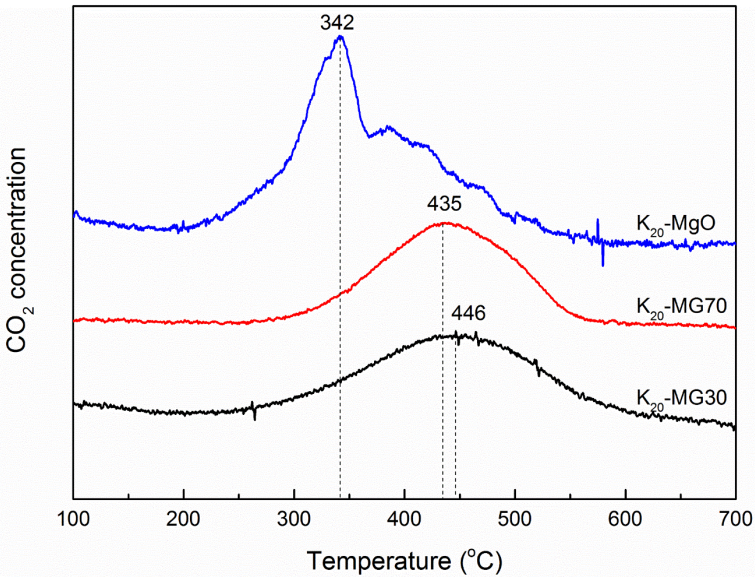

641

642 **Fig. 8. Difference spectra between the CO_2-TPD and thermal decomposition**

643 **spectra.**

644

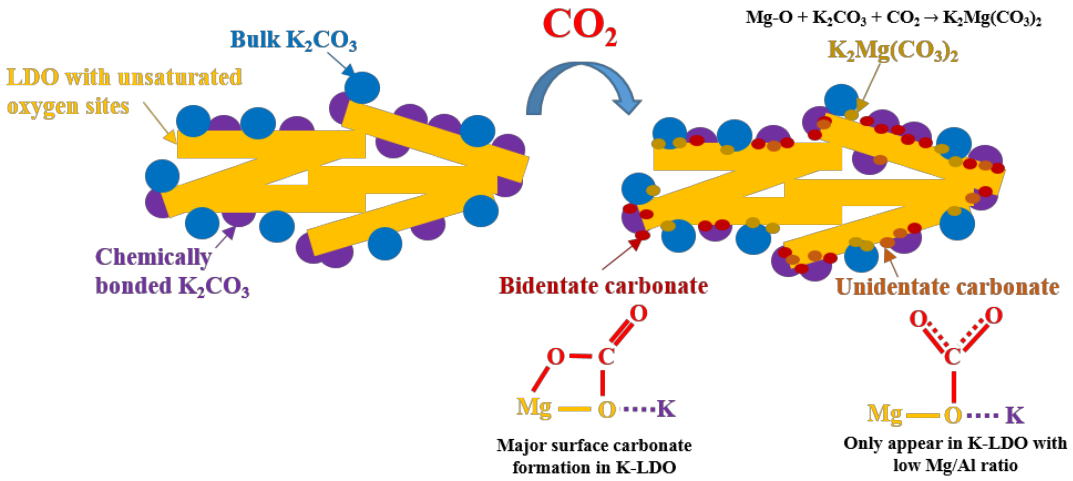

645

646 **Fig. 9. Schematic illustration of the possible CO_2 adsorption routes of K-LDOs.**

647

648

649

650